Tuning Fe-Se tetrahedral frameworks by a combination of $[Fe(en)_3]^{2+}$ cations and Cl^- anions

Eranga H. Gamage,[a,b] Joshua T. Greenfield,[c] Colin Unger,[c] Saeed Kamali,[d,e] Judith K. Clark,[f] Colin P. Harmer,[a,b] Liang Luo,[b,g] Jigang Wang,[b,g] Michael Shatruk,[f,h] Kirill Kovnir [a,b,*]

[a] *Department of Chemistry, Iowa State University, Ames, Iowa 50011, USA*

[b] *Ames Laboratory, U.S. Department of Energy, Ames, Iowa 50011, USA*

[c] *Department of Chemistry, University of California, Davis, Davis, CA 95616, USA*

[d] *Mechanical, Aerospace & Biomedical Engineering Department, University of Tennessee Space Institute, Tullahoma, TN 37388, USA*

[e] *Department of Physics and Astronomy, Middle Tennessee State University, Murfreesboro, TN 37132, USA*

[f] *Department of Chemistry and Biochemistry, Florida State University, Tallahassee, FL 32306, USA*

[g] *Department of Physics and Astronomy, Iowa State University, Ames, Iowa, 50011, USA*

[h] *National High Magnetic Field Laboratory, 1800 E Paul Dirac Dr, Tallahassee, FL 32310, USA*

ABSTRACT

A one-dimensional (1D) chain compound $[Fe(en)_3]_3(FeSe_2)_4Cl_2$ (*en* = ethylenediamine), featuring tetrahedral $FeSe_2$ chains separated by $[Fe(en)_3]^{2+}$ cations and Cl^- anions, has been synthesized by a low temperature solvothermal method using simple starting materials. The degree of distortion in the Fe-Se backbone is similar to previously reported compounds with isolated 1D $FeSe_2$ chains. ^{57}Fe Mössbauer spectroscopy reveals the mixed-valent nature of $[Fe(en)_3]_3(FeSe_2)_4Cl_2$ with Fe^{3+} centers in the $[FeSe_2]^-$ chains and Fe^{2+} centers in the $[Fe(en)_3]^{2+}$ complexes. SQUID magnetometry indicates that $[Fe(en)_3]_3(FeSe_2)_4Cl_2$ is paramagnetic with a reduced average effective magnetic moment, μ_{eff}, of 9.51 μ_B per formula, and a negative Weiss constant, θ, −10.9(4) K, indicating antiferromagnetic (AFM) nearest neighbor interactions within the $[FeSe_2]^-$ chains. Weak antiferromagnetic coupling between chains, combined with rather strong *intra*chain AFM coupling leads to spin-glass behavior at low temperatures, as indicated by a frequency shift of the peak observed at 3 K in AC magnetic measurements. A combination of $[Fe(en)_3]^{2+}$ and Cl^- ions is also capable of stabilizing mixed-valent 2D Fe-Se puckered layers in the crystal structure of $[Fe(en)_3]_4(Fe_{14}Se_{21})Cl_2$, where $Fe_{14}Se_{21}$ layers have a unique topology with large open pores. Property measurements of $[Fe(en)_3]_4(Fe_{14}Se_{21})Cl_2$ could not be performed due to the inability to either grow large crystals or synthesize this material in single-phase form.

INTRODUCTION

Low-dimensional transition metal chalcogenides have been intensively investigated in the past decade due to their vast structural diversity resulting in interesting superconducting and magnetic properties. Binary tetragonal iron sulfide and selenide exhibit superconducting properties with critical temperatures (T_c) below 10 K.[1–4] The layered structure makes these compounds suitable candidates for intercalation of guest species which helps tune their properties. Many researchers have explored layered binary iron chalcogenides as parent compounds to understand their intercalation chemistry and structure-properties relationships.[5–7] Increasing the interlayer distance and valence electron concentration by the introduction of electropositive cations such as Li^+, Na^+, K^+, Ca^{2+}, Sr^{2+} or Ba^{2+} raises the T_c to 30-46 K.[8–10] Intercalation of LiFe(OH) layers between FeSe layers gives rise to layered materials with magnetic ordering at ~12 K.[11] Superconducting critical temperatures exceeding 40 K have been achieved by displacing Fe atoms from the LiFe(OH) layers to occupy Fe site vacancies in the selenide layers.[12,13] While superconducting phases containing alkali metals and ammonia have been reported,[14] there are few detailed structural reports for such compounds. Clarke *et al.* reported the first reliable crystal structure determination of Li-ammonia intercalate in FeSe with T_c as high as 43 K,[7] as well as *in situ* characterization of the reactions of Li/NH_3 with FeSe using X-ray and neutron diffraction.[15] Insertion of transition metal coordination complexes with bulky ligands between the Fe chalcogenide layers allows further expansion of the interlayer space[16],[17] and contributes in tuning interactions of Fe-amine complexes with chalcogenide fragments.[18–20] Ethylenediamine (*en*) has been widely used as both a bidentate ligand and a solvent in the synthesis of such materials due to its versatility, high tendency to coordinate with transition metals and compatibility with Fe-based chalcogenides.[20–22]

In addition to layered chalcogenides, low-dimensional 1D hybrid metal chalcogenides are accessible by a solvothermal approach. For example, Goldberger *et al.* succeeded in the dimensional reduction of 2D TiQ_2 (Q = S, Se) into hybrid 1D structures.[23–25] We have shown that antiferromagnetic 1D $[FeSe_2]^-$ chains can be connected by $[Fe(en)_2]^{2+}$ units into a 3D framework in the crystal structure of $[Fe(en)_2](FeSe_2)_2$.[26] Using tridentate diethylenetriamine (*dien*), another quasi-1D compound, $[Fe(dien)_2](FeSe_2)_2$ was obtained, where $[FeSe_2]^-$ chains are completely isolated and only weak N–H···Se hydrogen bonding interactions are present between $[FeSe_2]^-$ chains and $[Fe(dien)_2]^{2+}$ complexes.[27] Purely inorganic compounds with antiferromagnetic $[FeS_2]^-$ or $[FeSe_2]^-$ 1D chains separated by alkali metal cations are also known, such as $AFeQ_2$ (A = K, Rb, Cs; Q = S, Se).[28–30] Recently, *Johrendt et al.* reported the synthesis of $[Fe(en)_3](FeSe_2)_2$ which contains $[FeSe_2]^-$ chains separated by non-covalently connected $[Fe(en)_3]^{2+}$ fragments, showing overall paramagnetic behavior.[31] In all hybrid compounds with $[FeSe_2]^-$ chains, the nature of the amine ligand determines the connectivity and properties of the Fe-chalcogenide fragments.

In this work, we used a combination of two spacer species, $[Fe(en)_3]^{2+}$ cations and Cl^- anions. In the crystal structures of $[Fe(en)_3]_3(FeSe_2)_4Cl_2$ and $[Fe(en)_3]_4(Fe_{14}Se_{21})Cl_2$, cationic and anionic species co-exist between infinite Fe-Se components, stabilizing 1D and novel 2D Fe-Se fragments. There are no covalent connections between the three components which are held together by hydrogen bonding, ionic, and van der Waals interactions. Synthesis and crystal

structures of $[Fe(en)_3]_3(FeSe_2)_4Cl_2$ and $[Fe(en)_3]_4(Fe_{14}Se_{21})Cl_2$, together with magnetic, Mössbauer, and vibrational properties of $[Fe(en)_3]_3(FeSe_2)_4Cl_2$, are reported here.

EXPERIMENTAL SECTION

Synthesis

Warning: Solvothermal reactions generate high pressures may produce various gaseous species, leading to the generation of extremely high pressures. Suitable high-strength reaction vessels are required to minimize the risk of an explosion.

Phase-pure $[Fe(en)_3]_3(FeSe_2)_4Cl_2$ was prepared by a solvothermal method. Stoichiometric amounts of iron (II) chloride tetra-hydrate (1 mmol) and selenium powder (1 mmol) were placed in a Teflon liner (liner volume 23 mL) which was subsequently filled with 10 mL of ethylenediamine up to a ~ 43% filling fraction. The liner was placed in a stainless-steel autoclave and sealed. The reaction vessel was then placed in the furnace and dwelled at 433 K for 5-7 days, taken out of the furnace and naturally cooled to room temperature in the fumehood. The products were filtered and washed with 200 proof ethanol and allowed to dry on air. The resulting sample consists of black shiny needles. For characterization and property measurements, $[Fe(en)_3]_3(FeSe_2)_4Cl_2$ samples synthesized using anhydrous iron (II) chloride and dry ethylenediamine under air-free conditions of Ar-filled glovebox were used.

A sample of reference compound, $[Fe(en)_3]Cl_2$, was synthesized under air-free conditions in the glovebox as described above by the reaction of anhydrous iron (II) chloride (1 mmol) with 10 mL of dry ethylenediamine and dwelling at 453 K for 2 days. Filtration with dry ethanol in the glovebox yielded an off-white powder which was assumed to be the target phase based on the resemblance of the powder X-ray diffraction (PXRD) pattern of the produced sample to that of $[Co(en)_3]Cl_2$ (Fig. S1).

$[Fe(en)_3]_4(Fe_{14}Se_{21})Cl_2$ crystals were selected from the products of a reaction containing iron, selenium, ammonium chloride, 1,10-phenanthroline in an excess of ethylenediamine. Synthesis of single-phase samples of this phase was unsuccessful, but we observed the formation of an analogous phase in small quantities by PXRD as one of the products in 1,10-phenanthroline -free conditions, namely in a solvothermal reaction of elemental iron with selenium in the presence of ammonium bromide in a solvent mixture of ethylenediamine and glycerol at 443 K.

More experimental details about the synthesis of both title compounds are provided in the Supporting Information.

Characterization

Samples of $[Fe(en)_3]_3(FeSe_2)_4Cl_2$ were stored and prepared for property measurements under argon. PXRD was performed on a bench top Rigaku 600 Miniflex with Cu-K_α radiation (λ = 1.54185 Å) and a Ni-K_β filter. Comparison of calculated and experimental patterns show a slight inconsistency in peak intensities due to preferred orientation of needle-like crystals (Fig. S2). The high background in the experimental pattern is due to fluorescence of Fe atoms in the sample upon exposure to incident Cu-K_α radiation.

Phase-pure $[Fe(en)_3]_3(FeSe_2)_4Cl_2$ sample was also characterized by *in-situ* synchrotron PXRD at beamline 17-BM-B (λ = 0.24153 Å) at the Advanced Photon Source located at Argonne National Laboratory, single crystal X-ray diffraction (SCXRD), ^{57}Fe Mössbauer spectroscopy, SQUID magnetometry, Energy Dispersive X-ray Spectroscopy (EDS), and Fourier Transform Infrared spectroscopy (FTIR) techniques. More information about the characterization techniques is given in the Supporting Information.

RESULTS AND DISCUSSION

Synthesis of $(FeSe_2)_4[Fe(en)_3]_3Cl_2$

$[Fe(en)_3]_3(FeSe_2)_4Cl_2$ was first synthesized as a byproduct while attempting to synthesize Fe selenides using 2,2'-bipyridine (*bpy*) as a ligand at 473 K. At first, it was assumed that *bpy* is required as a template to help this phase grow (Table S1). Later, however, reactions were conducted using $FeCl_2{\cdot}4H_2O$ in an excess of ethylenediamine at a lower temperature of 433 K. With an excess of the soluble iron salt, $[Fe(en)_3]_3(FeSe_2)_4Cl_2$ was obtained as the major product along with $[Fe(en)_3]Cl_2$. Synthesis using $FeCl_2{\cdot}4H_2O$ and Se in a 1:1 molar ratio and longer 7-day treatment produced an almost phase-pure sample of $[Fe(en)_3]_3(FeSe_2)_4Cl_2$ with unknown trace admixtures. Hence, *bpy* is not needed as a template for this phase to form. Here, all preparations and treatments of the starting materials were carried out on the bench top at ambient temperatures and humidity.

The use of NH_4Cl as a mineralizer to drive the reaction to completion and ensure crystallinity of the final product was not followed in the synthesis of $[Fe(en)_3]_3(FeSe_2)_4Cl_2$. This is quite different from our previous works[3,26,27] where the Fe starting material was in powdered metal form. In the current reactions, iron (II) chloride reacts with elemental Se to give the desired product without the need for additional reducing agents to form Se^{2-} ions. Use of iron (III) chloride and elemental Se as the starting materials in ethylenediamine solvent yields $[Fe(en)_3](FeSe_2)_2$ or $[Fe(en)_2](FeSe_2)_2$ as the main products. This clearly indicates that the oxidation of Fe^{2+}/Fe^{3+} (0.77 V) cannot solely cause a reduction of Se^0/Se^{2-} (–0.92 V).[32] It is hypothesized that ethylenediamine assists in this process as an unconventional reducing agent.[21] In fact, it was shown that S or Se can be reduced by ethylenediamine at solvothermal conditions.[33,34]

According to reactions conducted in the laboratory, $[Fe(en)_3]_3(FeSe_2)_4Cl_2$ is stable up to 473 K but forms with byproducts at elevated temperatures. 433 K was found to be the optimal temperature to synthesize this phase (Table S1). Starting from elemental Fe powder instead of iron chloride resulted in the formation of target phase but in the form of fine powders, even if an excess of NH_4Cl was used. Crystal growth is only favored in the presence of an excess of Cl^- in the reaction medium, from the dissolution of $FeCl_2{\cdot}4H_2O$, and above 423 K. An excess of selenium in the reaction mixture results in $[Fe(en)_3]Se_3$ admixtures, while 1-3 day thermal treatment gives FeSe and $FeSe_2$ byproducts.

The same optimized reaction was conducted in an argon-filled glovebox in an oxygen and moisture-free environment using dry ethylenediamine and anhydrous iron chloride, which resulted in the targeted phase with no admixtures (Table S1). This observation indicates that moisture does not play a role in the synthesis of $[Fe(en)_3]_3(FeSe_2)_4Cl_2$. However, regardless of the synthetic

conditions, it is necessary to store the sample in an inert atmosphere to prevent degradation and oxidation. The compound is air-stable for up to 3 days, but notable changes in the powder patterns were observed after 5 days (Fig. S3). Exposure to ambient conditions for up to 1 week leads to significant reduction in the intensity of the diffraction peaks, indicating that the material loses its crystallinity and converts to an amorphous phase. Low-intensity peaks appearing around ~26° cannot be assigned to known Fe-Se binaries, oxides or oxyhydroxides even though the color of the sample changed from black to red brown (Fig. S4). To investigate the thermal stability of $[Fe(en)_3]_3(FeSe_2)_4Cl_2$, decomposition studies were performed in a laboratory flow furnace under a N_2 flow, which indicated that the compound decomposes into binary FeSe and $FeSe_2$ between 383 – 393 K.

Elemental analysis with energy dispersive X-ray spectroscopy qualitatively detected the presence of Fe, Se, Cl, C, and N elements in the spectrum (Table S2). No oxygen was detected due to the storage of the sample under argon and the air-sensitive sample holder used to perform the measurements. A quantification of the acquired data gave an average heavy-element composition of $Fe_{6.8(2)}Se_8Cl_{2.2(3)}$, normalized to 8 Se atoms, which matches with the crystal structure of $[Fe(en)_3]_3(FeSe_2)_4Cl_2$. SEM images of the sample show needle-like crystals of different sizes ranging from 5 – 30 µm (Fig. S5).

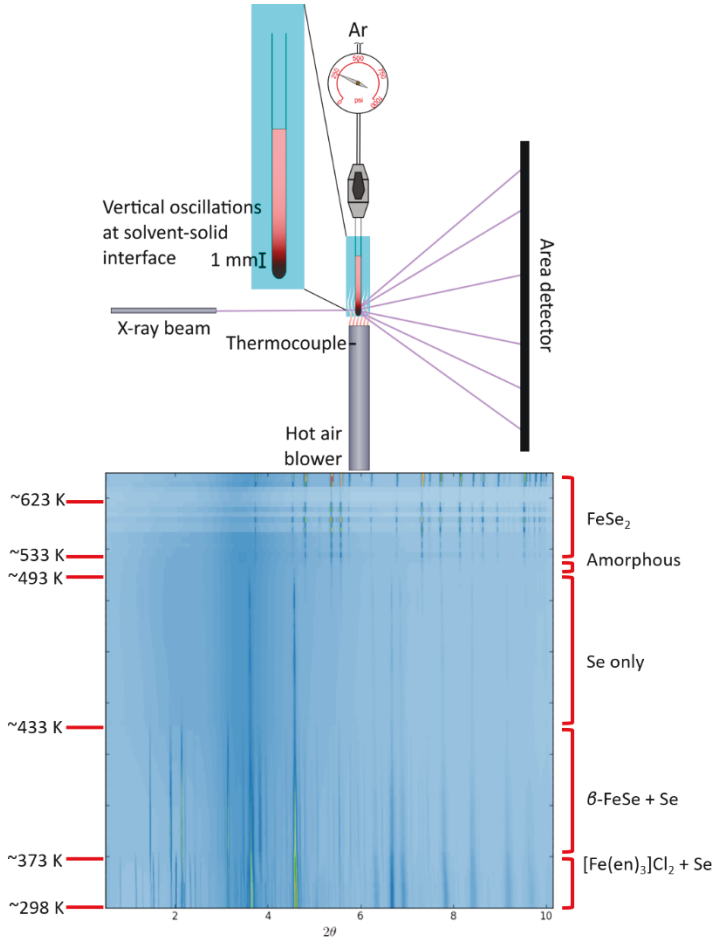

Figure 1. Top: Schematic of *in-situ* PXRD set-up for solvothermal systems at 17 BM-B. Bottom: Contour plot of the *in-situ* reaction of $FeCl_2 \cdot 4H_2O$ + Se in ethylenediamine in an open capillary under 500 psi pressurized nitrogen.

To investigate the formation of $[Fe(en)_3]_3(FeSe_2)_4Cl_2$, *in-situ* studies were done at the 17 BM-B beamline at the Advanced Photon Source at Argonne National Laboratory. The sample was contained in a capillary filled with solvent and subjected to 500 psi pressure of N_2 gas. Formation of $[Fe(en)_3]Cl_2$ by the reaction of $FeCl_2 \cdot 4H_2O$ with ethylenediamine was observed at room temperature (Fig. 1). Under a slow heating rate of 3 K/min, $[Fe(en)_3]Cl_2$ completely dissolved at ~373 K, followed by the formation of tetragonal β-FeSe (*P*4/*nmm*). This binary phase went into solution or amorphized at ~433 K and sustaining that temperature for 10 minutes did not show any sign of formation of the target phase, $[Fe(en)_3]_3(FeSe_2)_4Cl_2$. Only selenium diffraction peaks were observed until around its melting point of 493 K. Upon further heating, no crystalline diffraction peaks showed up in the 493-523 K range. Above 523 K, orthorhombic $FeSe_2$ (*Pnnm*) formed. Afterwards, no traces of the target phase were observed up to 623 K. The experiment was repeated with identical results, indicating that kinetic factors affect the reaction, which cannot be probed by short (2-4 hour) synchrotron experiments. To gain further insight into kinetic effects, laboratory reactions were conducted with short dwelling periods (0.5-2 hour), which yielded a mixture of compounds including $[Fe(en)_3]Se_3$ with no binary selenides or the target phase $[Fe(en)_3]_3(FeSe_2)_4Cl_2$ (Fig. S6). Therefore, it is evident that the reaction mixture should be subjected to longer in-furnace thermal treatment to form $[Fe(en)_3]_3(FeSe_2)_4Cl_2$. This assumption is supported with presence of binary FeSe and the target phase in the products of 1-3 days long reactions. Concentration effects may also play a role: for laboratory experiments, reactants were loaded in 20 mg/mL concentrations, while for synchrotron experiments, the volume is limited, and much larger concentrations of 5000 mg/mL were used.

Crystal Structure

$[Fe(en)_3]_3(FeSe_2)_4Cl_2$ crystallizes in the monoclinic space group *C*2/*c* (No. 15), with cell parameters of a = 23.212(4) Å, b = 11.277(2) Å, c = 19.767(4) Å, and β = 90.124(2)° and consists of $[FeSe_2]^-$ chains that propagate along the [010] direction. The chains are separated by $[Fe(en)_3]^{2+}$ cations and charge-balancing chloride anions (Fig. 2A). There are two different types of Fe atoms in the crystal structure. Fe1 and Fe2 atoms are coordinated by four Se atoms each, forming $FeSe_4$ tetrahedra, which share opposite edges to form the $[FeSe_2]^-$ chains (Fig. 2B). The $FeSe_4$ tetrahedra are distorted, with an average Fe-Se distance of 2.385(5) Å. The shortest $Fe^{complex}$-Fe^{chain} distance is 5.275(7) Å, which is much longer than the shortest *intra*chain Fe-Fe distance of 2.903(1) Å, while the shortest Se-Se distance is 3.678(1) Å. The Fe3 and Fe4 atoms are octahedrally coordinated by three bidentate *en* ligands (Figs. 2B and 2C). The anionic chains and cationic complexes are not covalently connected (Fig. 2D). The average Fe-N distance is 2.204(7) Å, which is indicative of the high spin Fe^{2+} ion, because low-spin Fe^{2+} or any Fe^{3+} typically exhibit shorter Fe-N distances of ≤ 2.0 Å.[35–37] Charge-balancing Cl^- ions occupy *4e* sites in the structure and are surrounded by $[Fe(en)_3]^{2+}$ complexes (Figs. 2B and 2D), forming N-H···Cl hydrogen bonding at distances of 2.42 – 2.71 Å for H···Cl. The Cl^- anions are arranged in channels along the [111]

direction. The crystal structure is additionally supported by weak N-H···Se interactions with H···Se distances of 2.61 Å.

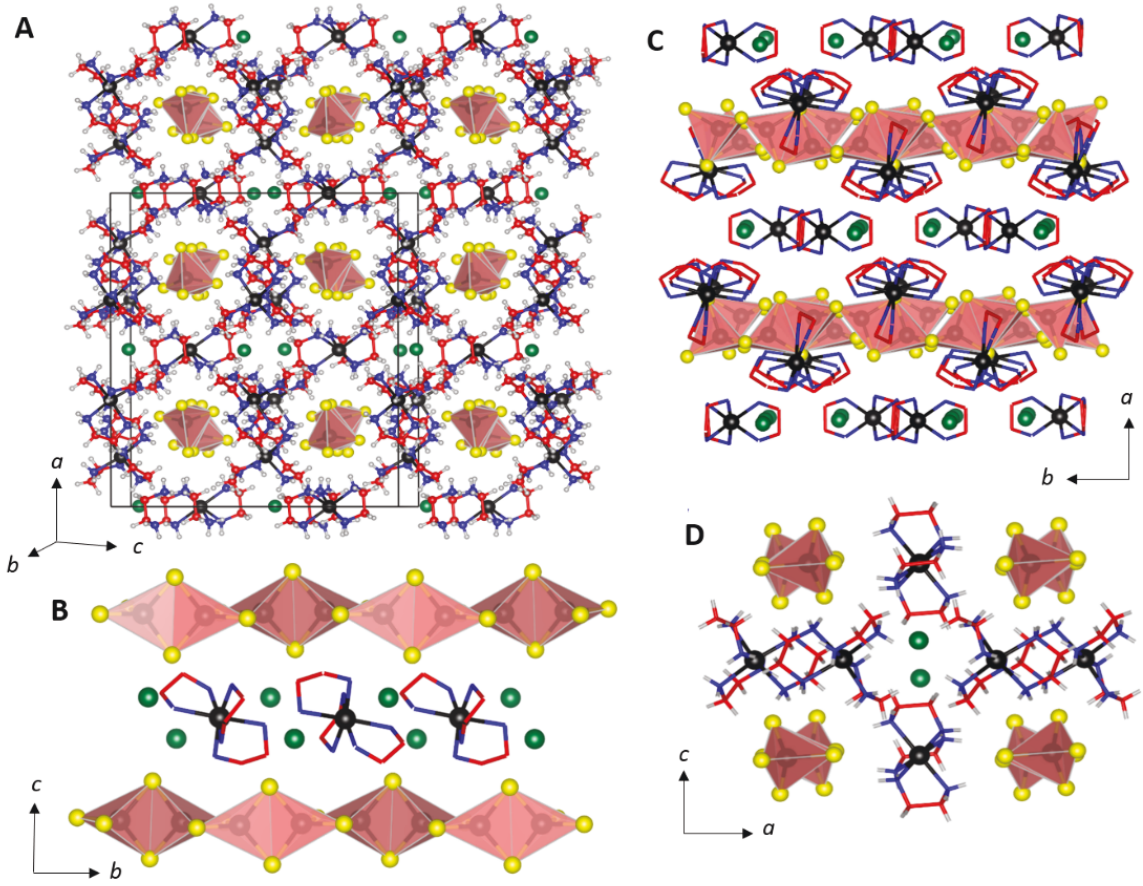

Figure 2. Crystal structure of $[Fe(en)_3]_3(FeSe_2)_4Cl_2$ **A)** General view along [010] direction **B-D)** fragments showing relative positions of chains, *tris*-en complexes and Cl^- anions showed along different crystallographic directions. Fe: black; Se: yellow; $FeSe_4$ tetrahedra: brown; N: blue; C: red; H: grey. Unit cell in **A)** is shown in black lines. In **B)** and **C)** hydrogen atoms are omitted for clarity.

The $[FeSe_2]^-$ chains composed of edge-sharing $FeSe_4$ tetrahedra in $KFeSe_2$ are almost linear with an Fe-Fe-Fe angle of 177.0° (Fig. 3, Table 1).[29] Replacement of K^+ ions with $[Fe(en)_2]^{2+}$ fragments, which are covalently bonded to Se atoms from two different chains, resulted in a slightly higher degree of distortion with an Fe-Fe-Fe angle of 176.4°.[26] The insertion of $[Fe(tren)]^{2+}$ complexes with two covalent connections to Se atoms from the same chain causes the highest degree of distortion, giving the smallest Fe-Fe-Fe angle of 157.8° and Fe-Se-Fe angle of 70.6°.[27] It is noteworthy how the angle between Se dihedral planes is decreased in the presence of complex-chain covalent bonds. The replacement of covalently bound $[Fe(en)_2]^{2+}$ fragments with non-covalently bound complexes, $[Fe(en)_3]^{2+}$ and $[Fe(dien)_2]^{2+}$, which exhibit only weak Se···H–N hydrogen bonding, results in a higher degree of chain distortion (Fig. 3, Table 1). A similar effect is observed for $[Fe(en)_3]_3(FeSe_2)_4Cl_2$, which demonstrates a significant degree of distortion of the

$[FeSe_2]^-$ chains with a smaller Fe-Fe-Fe angle and reduced dihedral angles between Se planes (Fig. 3, Table 1).

Another factor that could possibly play an important role in the distortions, is the oxidation states of Fe atoms in the chains. Presence of Fe^{2+} species can control the dihedral angles and lead to kinking of the Fe-Se chains. To further investigate the effects of electronic factors on the Fe-Se chains, bond valence sum (BVS)[38] analysis was performed to deduce the oxidation states of Fe atoms in the chains (Table 1). The calculations show that all the Fe^{chain} atoms in the discussed compounds bear +3 charge. This result is further confirmed for $[Fe(en)_3]_3(FeSe_2)_4Cl_2$ (current work), $[Fe(en)_2](FeSe_2)_2$[26] and $[Fe(tren)](FeSe_2)_2$[27] compounds by Mössbauer spectroscopy studies. Therefore, it is evident that the charge of Fe^{chain} atoms consistently remains +3 and what controls the dihedral angles of the Fe-Se chains is the steric factors arising from the amine-coordinated iron complexes rather than electronic factors. *Tris*-en complexes embedded between the Fe-Se chains may exhibit additional distortion as compared to such complexes in $[Fe(en)_3]Cl_2$. To study this, we used FTIR spectroscopy.

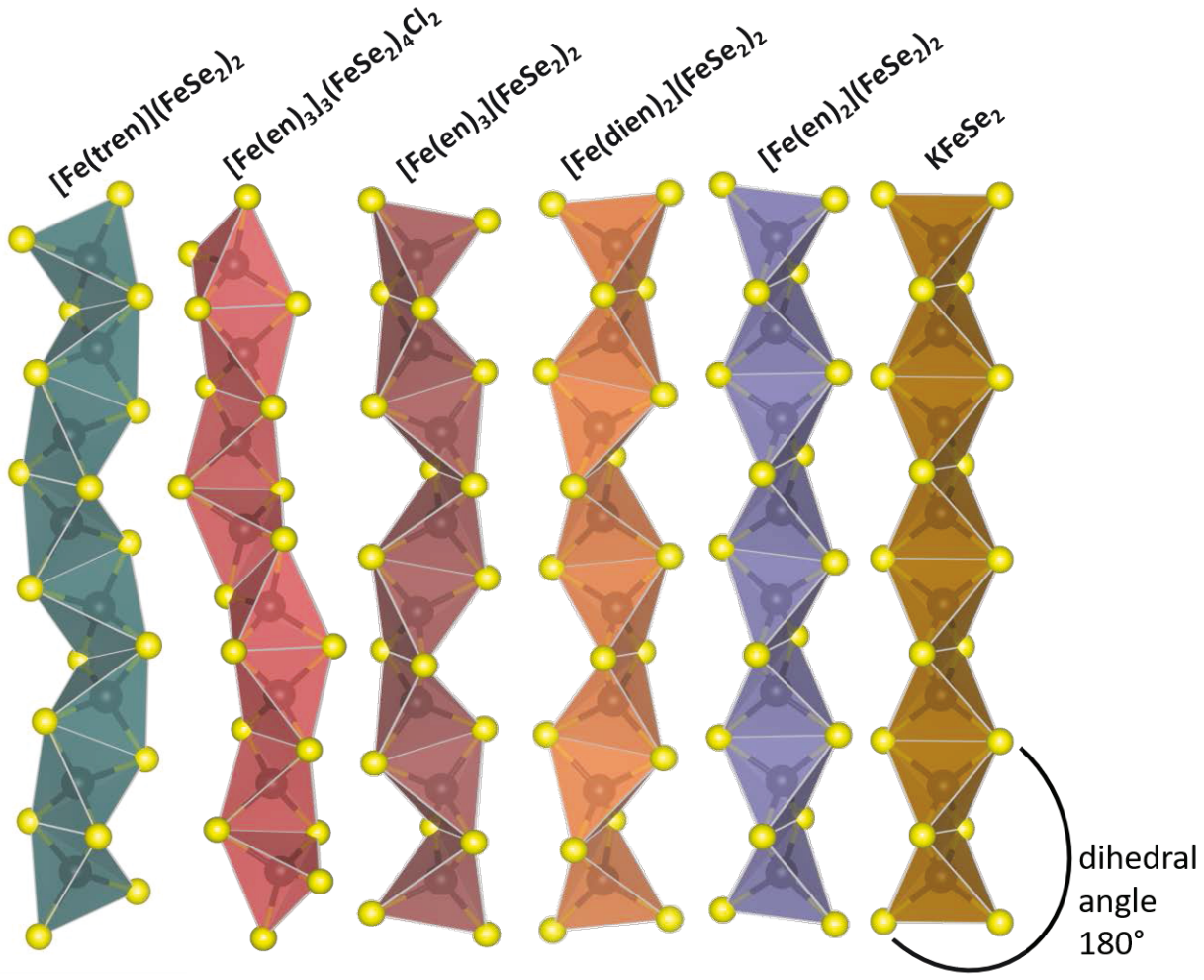

Figure 3. $[FeSe_2]^-$ chains from different crystal structures.

Table 1. Selected properties for $[FeSe_2]^-$ chains found in different compounds.

Structure [reference]	∠ Fe-Fe-Fe (°)	∠ Fe-Se-Fe (°)	Se planes dihedral ∠ (°)	Fe-Fe bond distance (Å)	Type of magnetic exchange	Calculated BVS of chain Fe atoms
$[Fe(tren)](FeSe_2)_2$ [27]	157.82	70.55 – 72.89	170.29	2.73 – 2.79	FM	Fe6 +3.11 Fe7 +3.19
$[Fe(en)_3]_3(FeSe_2)_4Cl_2$ [*current work*]	160.89(3)	73.98(4) – 76.64 (4)	176.68(7)	2.904(1) – 2.932(1)	AFM	Fe1 +3.01 Fe2 +3.02
$[Fe(en)_3](FeSe_2)_2$ [31]	164.41	77.49 – 77.51	180.0	2.95 – 2.98	AFM	Fe1 +3.03 Fe2 +3.09
$[Fe(dien)_2](FeSe_2)_2$ [27]	169.16	75.23 – 75.31	178.28	2.91 – 2.92	AFM	Fe1 +3.01
$[Fe(en)_2](FeSe_2)_2$ [26]	176.41	74.99 – 76.22	170.07	2.87 – 2.94	AFM	Fe1 +3.13
$KFeSe_2$ [29]	177.00	73.02	180.0	2.82	AFM	Fe1 +3.17

FTIR spectroscopy

Fourier Transform Infrared (FTIR) spectra of $[Fe(en)_3]_3(FeSe_2)_4Cl_2$ and $[Fe(en)_3]Cl_2$ were measured in the 400 – 4000 cm^{-1} range to compare bonding vibrational modes of the complexes (Fig. 4). The spectrum of solution-phase ethylenediamine was obtained from the NIST Chemistry WebBook, SRD 69.[39] $[Fe(en)_3]Cl_2$ is expected to have isolated *tris*-en complexes surrounded by Cl^- anions in analogy to $[Co(en)_3]Cl_2$.[40] A comparison of the spectra for $[Fe(en)_3]_3(FeSe_2)_4Cl_2$ and $[Fe(en)_3]Cl_2$ shows a significant restructuring of the N-H stretching region centered ~3250 cm^{-1} and a red shift in the N-H stretching and rocking bands of the $[Fe(en)_3]_3(FeSe_2)_4Cl_2$ spectrum, probably due to weak N-H···Se hydrogen bonding.[41] The low-frequency FTIR spectrum (Fig. S7) obtained in the 30-500 cm^{-1} range shows the $[Fe(en)_3]^{2+}$ chelate ring deformation and Fe-N vibrational modes appearing below 500 cm^{-1}.[42] According to Thornton *et al*. all the N-Fe-N bending frequencies show up in the ~100 – 300 cm^{-1} range.[43] Fe-Se lattice vibrations are expected to give bands below 100 cm^{-1} (Figure S7: inset), but we have insufficient experimental data for complete interpretation of those bands with certainty.

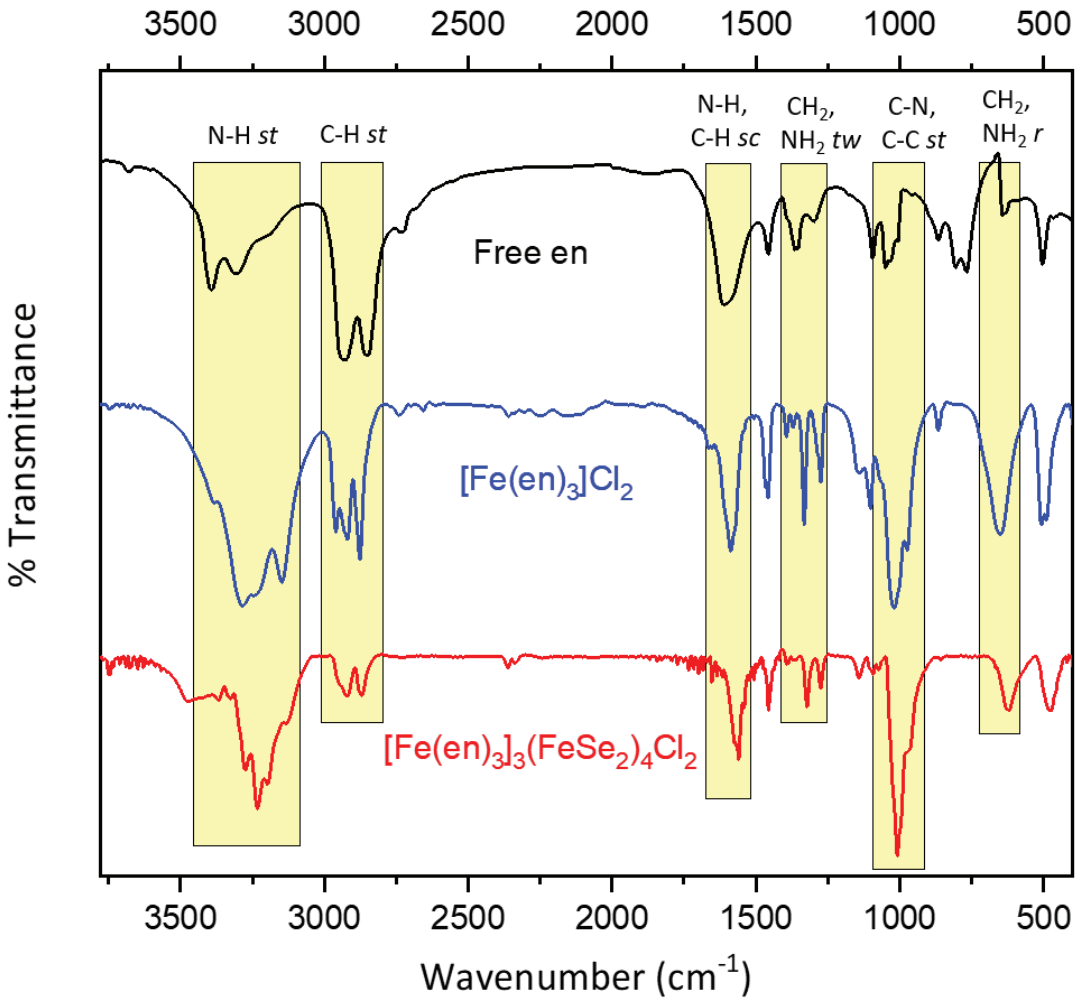

Figure 4. FTIR spectra of free ethylenediamine (*en*) (black), $[Fe(en)_3]Cl_2$ (blue) and $[Fe(en)_3]_3(FeSe_2)_4Cl_2$ (red). *st* = stretching, *sc* = scissoring, , *tw* = twisting, *r* = rocking.

^{57}Fe Mössbauer Spectroscopy

Based on crystal structure refinement, our compound contains four $[FeSe_2]^-$ units per three $[Fe(en)_3]^{2+}$ cations and two chloride anions, which suggests a charge of 3+ for Fe in the $FeSe_2$ chains: $[Fe^{2+}(en)_3]_3(Fe^{3+}Se^{2-}{}_2)_4(Cl^-)_2$. Mössbauer spectroscopy studies confirmed this assignment of the formal oxidation states (Fig. 5, Table 2). Starting from the 6 K spectrum, the first component, Q_1, with a δ value of 0.36 mm/s and a ΔE_Q value of 0.43 mm/s, is the signal from tetrahedral Fe^{3+} ions.[44] This component has an intensity of 44% and a linewidth of 0.37 mm/s. The second component, Q_2, has δ of 1.13 mm/s and ΔE_Q of 1.80 mm/s, which are characteristic values for high-spin Fe^{2+}.[45] This component has an intensity of 56% and a linewidth of 0.49 mm/s.

The spectra measured at 100 K and 293 K are also best fitted as two doublets with drastically different parameters. The δ and ΔE_Q parameters determined for the Q_1 component at

293 K match those of the room temperature Mössbauer spectrum of $RbFeSe_2$.[46] The higher δ and ΔE_Q values of the Q_2 component are similar to those ($\delta = 0.88$ mm/s and $\Delta E_Q = 0.86$ mm/s) reported for $[Fe(en)_2](FeSe_2)_2$, which contains Fe^{2+} in a distorted octahedral environment of 4 N and 2 remote Se atoms.[26] As seen in Table 2, the δ values decrease with increasing temperature for both components, in accordance with the temperature-dependent contribution to the centroid shift caused by the second order Doppler effect. The relative intensity of the first component increases with temperature, while the relative intensity of the second component decreases. This indicates a rapid decrease in the recoil free fraction of the second component, which results in the redistribution of relative intensities.[47] Comparison of the spectra at three different temperatures shows how the ΔE_Q value for the second component decreases from 1.80 mm/s at 6 K to 0.60 mm/s at 293 K. This decrease in ΔE_Q, most likely stems from a change in the electron density distribution over asymmetrically occupied degenerate orbital states of Fe^{2+} that is temperature sensitive.[48]

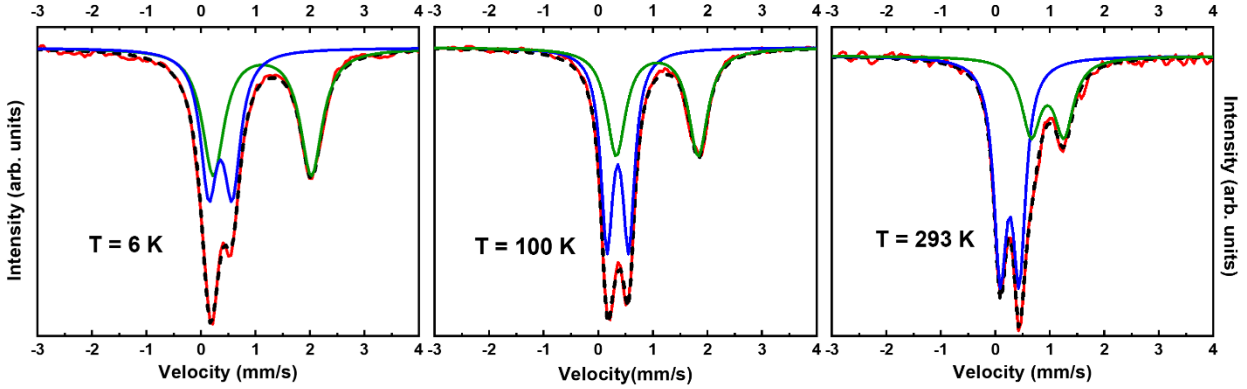

Figure 5. ^{57}Fe Mössbauer spectra for $[Fe(en)_3]_3(FeSe_2)_4Cl_2$ measured at various temperatures. Experimental data: red; calculated spectrum: black dots; Fe^{3+}: blue; Fe^{2+}: green.

Table 2. Summary of refined Mössbauer parameters for $[Fe(en)_3]_3(FeSe_2)_4Cl_2$, measured at 6 K, 100 K, and 293 K: centroid shift, δ, quadrupole splitting, ΔE_Q, full-width at half-maximum, Γ, and intensity, I, of the different components, Q_1, first row, and Q_2, second row. Estimated standard deviations are $I \pm 2\%$, δ and $\Delta E_Q \pm 0.005$ mm/s, and $\Gamma \pm 0.05$ mm/s.

	Temperature	6 K	100 K	293 K
Component Q_1 HS-Fe^{3+}	δ_1 (mm/s)	0.358	0.358	0.264
	ΔE_{Q1} (mm/s)	0.432	0.398	0.350
	Γ_1 (mm/s)	0.37	0.27	0.28
	I_1 (%)	44	53	65
Component Q_2 HS-Fe^{2+}	δ_2 (mm/s)	1.126	1.080	0.958
	ΔE_{Q2} (mm/s)	1.801	1.503	0.601
	Γ_2 (mm/s)	0.49	0.42	0.42
	I_2 (%)	56	47	35

Magnetic properties

$[Fe(en)_3]_3(FeSe_2)_4Cl_2$ exhibits paramagnetic behavior without signs of magnetic ordering down to 1.8 K (Fig. 6). The FC and ZFC magnetic susceptibility (χ) curves coincide at high temperatures and show a small divergence at lower temperatures (Fig. 6). A modified Curie-Weiss fit, $1/\chi = 1/(\chi_o + C/(T-\theta))$, which accounts for a temperature-independent paramagnetic contribution, χ_o, gave the best-fit values of $\chi_o = 0.065(2)$ emu/mol, $C = 11.3(7)$ emu·K/mol and $\theta = -10.9(4)$ K. The negative value of the asymptotic Weiss temperature indicates antiferromagnetic (AFM) interactions between the nearest-neighbor Fe^{3+} ions within the $[FeSe_2]^-$ chains. The intrachain Fe--Fe exchange interaction is affected by a combination of several factors including Fe-Fe distances, Fe-Fe-Fe angles and Fe-Se-Fe angles in the chains.

For $[Fe(en)_3]_3(FeSe_2)_4Cl_2$, the average Fe-Fe distance is ~2.9 Å, while the Fe-Se-Fe angles vary from 73.98(4)° – 76.64(4)° (Table 1). The AFM interactions in $[Fe(en)_3]_3(FeSe_2)_4Cl_2$ are significantly weaker than those in the previously reported $[Fe(en)_2](FeSe_2)_2$ with $\theta = -105(8)$ K.[26] The stronger exchange in $[Fe(en)_2](FeSe_2)_2$ can be explained by the minimal distortion from linear chains resulting from complex-chain covalent bonding and slightly shorter Fe-Fe distances of 2.87 Å (Table 1). On the contrary, $[Fe(tren)](FeSe_2)_2$, which has two covalent bonds from $[Fe(tren)]^{2+}$ to Se atoms in the same chain, has the highest degree of distortion and shows strong ferromagnetic nearest-neighbor interactions ($\theta = +145$ K).[27] A change in the type of exchange may have been caused by the bending of chains and shortening of Fe-Fe distances to 2.73 – 2.79 Å in $[Fe(tren)](FeSe_2)_2$. Therefore, the type of Fe-Fe magnetic interactions in $[FeSe_2]^-$ chains is sensitive to the bending of the chain and, correspondingly, to the Fe-Fe interatomic distances. In the absence of covalent interactions between $[FeSe_2]^-$ chains and amine complexes, chain distortion was observed without significant shortening of the Fe-Fe distances (Table 1) resulting in weaker AFM interactions in the crystal structures of $[Fe(en)_3](FeSe_2)_2$ ($\theta = -6.4$ K)[31] and $[Fe(dien)_2](FeSe_2)_2$ ($\theta = -5.2$ K).[27] The novel compound $[Fe(en)_3]_3(FeSe_2)_4Cl_2$ exhibits intermediate Fe-Se chain distortion with relatively long Fe-Fe distances, comparable to those in $[Fe(en)_3](FeSe_2)_2$ and $[Fe(dien)_2](FeSe_2)_2$, and thus the observed magnetic nearest neighbor interactions are similar for the three compounds with non-covalent bonding between Fe-Se chains and Fe amine complexes.

An effective magnetic moment, μ_{eff}, obtained from the modified Curie-Weiss fit is 9.51 μ_B, corresponding to χT of 11.3 emu·K/mol, per formula unit, which is lower than the expected value of $\mu_{eff} = 14.57$ μ_B, corresponding to χT of 26.5 emu·K/mol, resulting from the presence of four high-spin Fe^{3+} ions (5.92 μ_B, $S = 5/2$) and three high-spin Fe^{2+} ions (4.90 μ_B, $S = 2$) in $[Fe(en)_3]_3(FeSe_2)_4Cl_2$. A similar reduced moment was observed for other compounds with $[FeSe_2]^-$ chains.[26,27,29,31] One possible explanation for this is the partial quenching of the Fe^{3+} magnetic moment due to the covalency of the Fe-Se bonds.

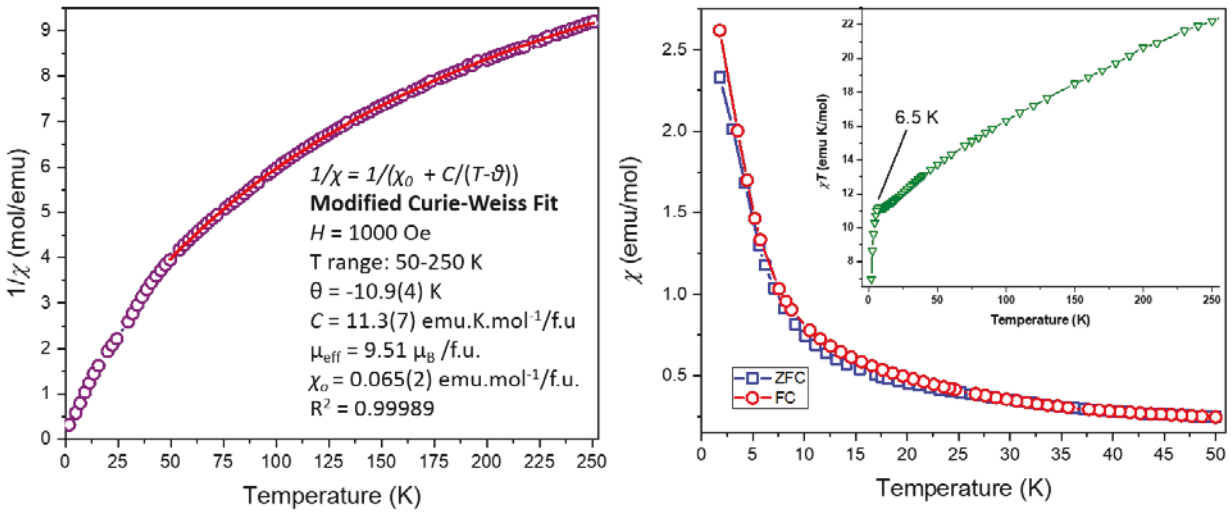

Figure 6. Left: Temperature-dependence of inverse magnetic susceptibility ($1/\chi$) for $[Fe(en)_3]_3(FeSe_2)_4Cl_2$ in an applied field of 1000 Oe. Modified Curie-Weiss fitting in 50-250 K range is shown with a red line. Right: Temperature-dependence of ZFC/FC susceptibility under an applied field of 100 Oe. Inset: Temperature-dependence of χT, revealing an anomaly at 6.5 K.

The χT vs. T dependence (Fig. 6 inset) shows a steady decrease from 250 K to ~10 K, in agreement with the presence of the temperature-independent contribution and AFM interactions. A sharp drop in χT was observed at 6.5 K. Along with the slight divergence between the ZFC and FC susceptibility curves observed in that temperature range, such behavior prompted us to investigate a possible spin glass state. AC susceptibility measurements revealed that both the real (χ') and imaginary parts (χ'') of the susceptibility show frequency dependent shifts in the peak position and intensity (Fig. 7, Fig. S8). The empirical Mydosh parameter (φ), calculated from the peak of χ' frequency dependence, is 0.03, which is in the typical range for spin glasses (0.004-0.08).[49] This spin glass state is not associated with a substitutional disorder as observed in substituted spinels[50,51] or ternary phosphides.[52] The origin of this spin glass nature can be attributed to the weak AFM coupling between the chains, as contrasted with rather strong *intra*chain AFM coupling. The weak super-exchange through the $[Fe(en)_3]^{2+}$ cations causes *inter*chain AFM correlations that are frustrated and lead to the spin glass state. To the best of our knowledge, AC magnetic studies have not been performed for other compounds with similar chains.[26,27,31]

The isothermal field-dependence of magnetization measured at 1.8 K exhibits a non-saturated behavior with a maximum magnetization value of 9.6 μ_B/f.u. achieved at the highest applied field of 70 kOe (Fig. 7). This value is substantially smaller than the total saturation value of 32 μ_B/f.u expected for the fully aligned high-spin moments of all Fe centers. The relatively small value of the maximum magnetization indicates strong AFM interactions in the spin glass state, which cannot be overcome by an applied field up to 70 kOe.

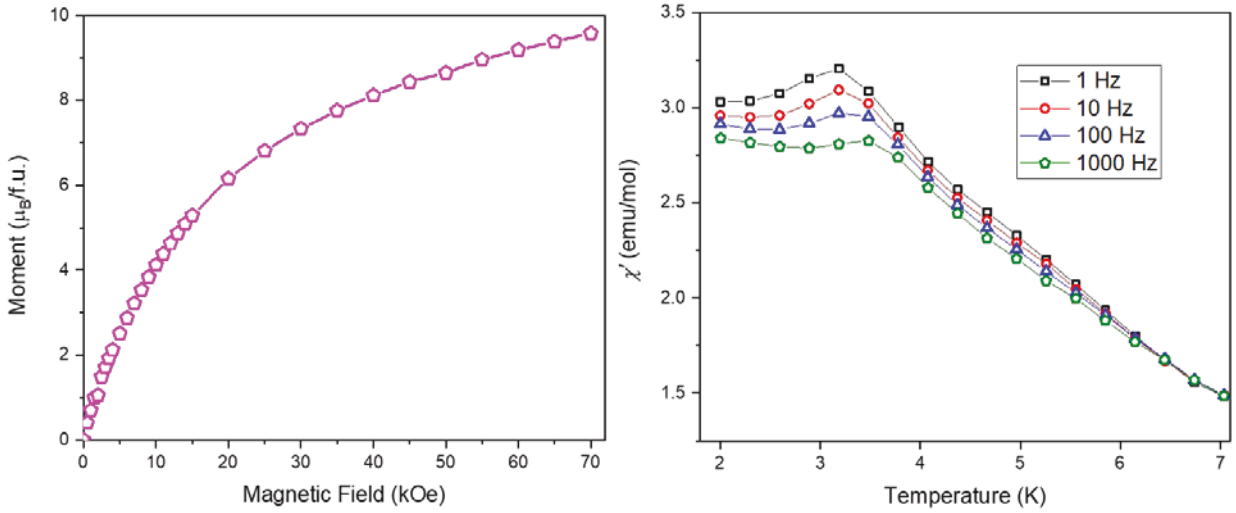

Figure 7. Left: Isothermal field-dependence of magnetization at 1.8 K for $[Fe(en)_3]_3(FeSe_2)_4Cl_2$. Right: Real part of AC susceptibility (χ') oscillating at a frequency ranging from 1 to 1000 Hz.

$[Fe(en)_3]_4(Fe_{14}Se_{21})Cl_2$

$[Fe(en)_3]_4(Fe_{14}Se_{21})Cl_2$ crystals were selected from the products of the reaction of iron and selenium with an excess of ethylenediamine in the presence of ammonium chloride and 1,10-phenanthroline. The sample consisted of uniform needle-like crystals, the vast majority of which were $[Fe(en)_2](FeSe_2)_2$[26] according to single-crystal and powder X-ray diffraction. Careful inspection of samples revealed that a small number of crystals cleaved differently, suggesting a layered structure. These crystals were determined to be $[Fe(en)_3]_4(Fe_{14}Se_{21})Cl_2$ by reproducible single-crystal X-ray diffraction experiments. The concentration of these crystals in the sample was extremely low, which explains why the presence of $[Fe(en)_3]_4(Fe_{14}Se_{21})Cl_2$ was not detected by PXRD. Attempts to produce single-phase samples of this compound were unsuccessful, but we observed the formation of an analogous phase by PXRD as one of the products in phenanthroline-free reactions, indicating that phenanthroline is not required to form this phase (Table S1). We hypothesize, based on our *in-situ* results that tetragonal *β*-FeSe forms first under the reaction conditions. Further treatment of this phase with solutions containing an excess of *en* and $[Fe(en)_3]^{2+}$ complexes results in the formation of layered $[Fe(en)_3]_4(Fe_{14}Se_{21})Cl_2$, which in turn converts into the more stable chain compound $[Fe(en)_3]_3(FeSe_2)_4Cl_2$.

$[Fe(en)_3]_4(Fe_{14}Se_{21})Cl_2$ crystallizes in the monoclinic space group *P*2/*n* (No. 13), with unit cell parameters of a = 16.521(3) Å, b = 8.833(2) Å, c = 30.132(6) Å, and β = 104.307(3)°. This crystal structure contains three structural subunits; $Fe_{14}Se_{21}$ puckered layers, $[Fe(en)_3]^{2+}$ complexes, and chloride anions. $Fe_{14}Se_{21}$ layers are stacked along the [100] with the interlayer space occupied by $[Fe(en)_3]^{2+}$ complexes and chloride anions. The latter is surrounded by *tris*-en complexes which do not appear anywhere near the $Fe_{14}Se_{21}$ fragments (Figure 8).

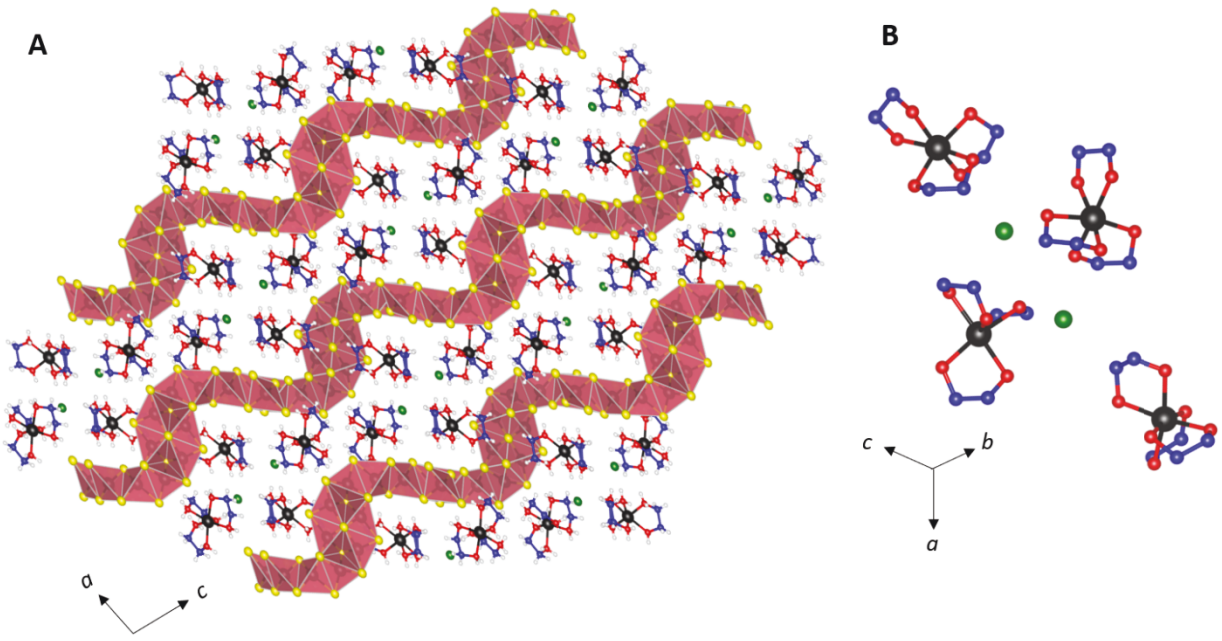

Figure 8. Crystal structure of $[Fe(en)_3]_4(Fe_{14}Se_{21})Cl_2$. **A)** General view showing puckered $Fe_{14}Se_{21}$ layers in polyhedral representation. **B)** Local coordination of Cl^- surrounded by $[Fe(en)_3]^{2+}$. Fe: black; Se: yellow; $FeSe_4$ tetrahedra: brown; N: blue; C: red; H: grey; Cl: green. In **B)** H atoms are omitted for clarity.

The two-dimensional $Fe_{14}Se_{21}$ layers are more complex than the simple double tetrahedral chains found in $Ba_2Fe_2Se_3$[53,54] and $[Fe(en)_3]_2(Fe_2Se_3)_4en$.[31] Segments of Fe-Se chains are found to grow both parallel and perpendicular to $[Fe(en)_3]^{2+}$ planes and consist of distorted $FeSe_4$ tetrahedra sharing three edges (Fig 9A). Fe1, Fe2, and Fe3 are found in parallel segments while Fe5, Fe6, and Fe7 are found in perpendicular segments, with Fe4 connecting pairs of segments together. Interestingly, the parallel segments possess Se atoms with multiple bridging modes including μ^2, μ^3, and μ^4 (Fig. 9B, Table S3). Increasing coordination numbers for Se result in increasing Fe-Se distances. The Se1 and Se5 atoms with μ^2 coordination are located near the edges of the Fe-Se backbone and have shorter Fe-Se distances (2.302(1) – 2.326(1) Å), while the μ^3-bridging Se3 and Se4 atoms show longer Fe-Se distances (2.369(1) – 2.466(1) Å). For μ^4 – Se2 atoms, the Fe-Se distance varies in the range of 2.434(1) – 2.456(1) Å and Se-Fe-Se angles in the tetrahedra vary from 105.49(3) to 114.50(3)°. This clearly shows the degree of distortion in the $FeSe_4$ tetrahedra with respect to β-FeSe, which has $d_{Fe\text{-}Se}$ = 2.393 Å and ∠Se–Fe–Se =104.0 – 112.3°.[55]

The perpendicular segments have different bond distances and angles compared to the parallel segments (Fig 9C, Table S3). There, μ^4 – Se10 atoms have Fe-Se bond distances spanning from 2.456(1) – 2.712(2) Å and Se-Fe-Se angles in the $FeSe_4$ tetrahedra vary from 102.84(3) – 117.55(3)°. The μ^2 – Se7, Se8 and Se11 atoms exhibit Fe-Se distances of 2.341(1) – 2.387(1) Å, and the μ^3 – Se6 and Se9 atoms show distances of 2.386(1) – 2.431(1) Å. These dimensions vary more significantly than those in the parallel segments mentioned above. The Fe atoms in $[Fe(en)_3]^{2+}$ complexes are octahedrally coordinated by the six N atoms of three *en* molecules. These units are stabilized between $Fe_{14}Se_{21}$ fragments by Se···H–N hydrogen bonds facilitated by a minimum hydrogen bonding distance of 2.749 Å between $[Fe(en)_3]^{2+}$ and μ^2 – Se atoms. Charge-

balancing chlorides link to the surrounding $[Fe(en)_3]^{2+}$ via Cl···H–N hydrogen bonds at distances ranging from 2.258 – 2.468 Å. In the $[Fe(en)_3]^{2+}$ fragments, the average Fe-N bond distance is 2.22(2) Å, which is comparable to the same distance in $[Fe(en)_3]_3(FeSe_2)_2$. These distances match with the high spin Fe-N bond distances found in octahedral complexes.[35]

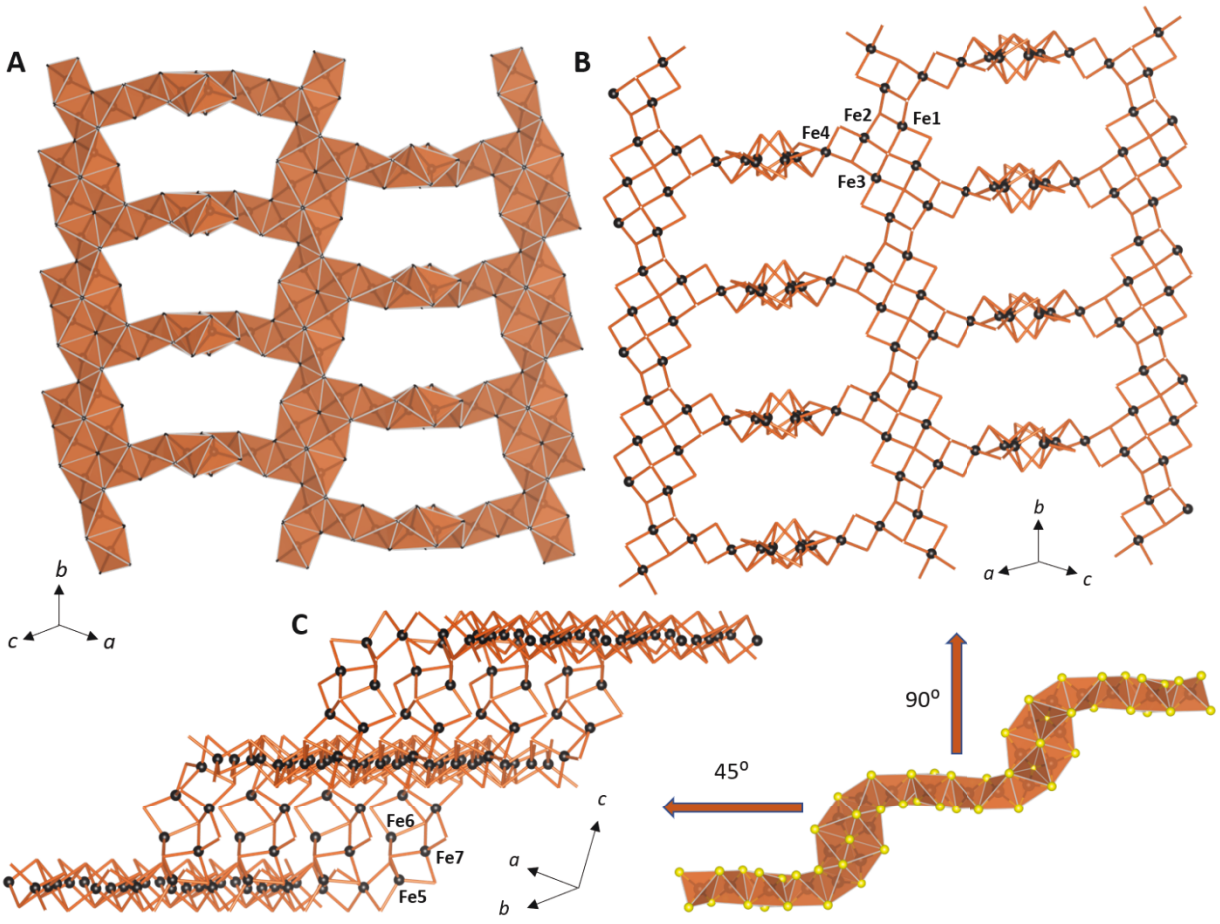

Figure 9. Detailed structure of $Fe_{14}Se_{21}$ layer. **A)** Polyhedral representation along the diagonal axis. **B)** and **C)** Ball-and-stick representations with Fe atoms shown as black spheres emphasizing bonding in parallel segments **(B)** and perpendicular segments **(C)**. Unique Fe crystallographic sites are labeled in **B)** and **C)**.

According to the formula unit of this structure, the $Fe_{14}Se_{21}$ backbone should have mixed-valent Fe atoms in the layer, unlike the sole Fe^{3+} in $FeSe_2$ chains in $[Fe(en)_3]_3(FeSe_2)_4Cl_2$. For charge balancing purposes, $[Fe(en)_3]^{2+}$ complexes are assumed to have +2 charge providing a balanced formula as $([Fe(en)_3]^{2+})_4(Fe_{14}Se_{21})^{6-}(Cl^-)_2$. Assuming a –2 oxidation state for Se, Fe atoms in the $Fe_{14}Se_{21}$ layer should have an average oxidation state of +2.57. This implies six Fe^{2+} and eight Fe^{3+} ions in the $Fe_{14}Se_{21}$ motif, giving the formula unit as $([Fe(en)_3]^{2+})_4[(Fe^{2+})_6(Fe^{3+})_8(Se^{2-})_{21}](Cl^-)_2$. The Fe^{3+}-Se distance in $[Fe(en)_3](FeSe_2)_2$ is between 2.339(1) – 2.432(1) Å and the Fe^{2+}-Se distance in β-FeSe is 2.3846 Å.[3] While comparing bond distances is not enough for a formal assignment of oxidation states of the Fe atoms in the Fe-Se layers, an analysis of the $FeSe_4$ tetrahedral volume is insightful.

Table 3. Volumes of $FeSe_4$ tetrahedra and bond valence sum (BVS)[38] for all Fe atoms in the $Fe_{14}Se_{21}$ layer in the crystal structure of $[Fe(en)_3]_4(Fe_{14}Se_{21})Cl_2$. Fe4 connects parallel and perpendicular fragments.

	Atom	Volume of $FeSe_4$ ($Å^3$)	Calculated BVS	Tentative oxidation state
Parallel segment	Fe1	6.97	+2.99	+3
	Fe2	6.92	+3.06	+3
	Fe3	7.03	+2.94	+2
	Fe4	6.99	+2.90	+2
Perpendicular segment	Fe5	6.86	+3.08	+3
	Fe6	7.05	+2.56	+2
	Fe7	6.98	+2.95	+3

The volume of $Fe^{2+}Se_4$ tetrahedra in β-FeSe is 6.93 $Å^3$ and that of $Fe^{3+}Se_4$ tetrahedra in $[Fe(en)_2](FeSe_2)_2$ is 6.76 $Å^3$, which indicates the expected shrinking in tetrahedral volume as the charge on the Fe atoms increase. However, the $Fe^{3+}Se_4$ tetrahedra in $[Fe(en)_3](FeSe_2)_2$ have a volume of 6.78 – 6.83 $Å^3$ due to distortion in the $FeSe_2$ chains.[31] In $[Fe(en)_3]_4(Fe_{14}Se_{21})Cl_2$, the $Fe^{3+}Se_4$ tetrahedra have volumes varying from 6.86 – 7.05 $Å^3$ (Table 3). The bond-valence sum analysis gives oxidation states for Fe ranging from +2.56 to +3.08 (Table 3). Fe6 has the largest tetrahedral volume and the lowest BVS of +2.56, indicating a +2 oxidation state. Fe5 and Fe2 have the smallest tetrahedral volumes and the largest BVS and can be assigned a +3 oxidation state. The other four Fe atoms have similar volumes and BVS, so the assignment of their oxidation states is speculative and solely based on the electron balanced assumption. This means that the $Fe_{14}Se_{21}$ layers may not have tetrahedral Fe atoms with stable oxidation states of +2 or +3, but instead the Fe atoms may have an intermediate oxidation state due to delocalized electron density. Another possibility is that the $Fe_{14}Se_{21}$ layers are not charge balanced and have metallic properties. Unfortunately, Mössbauer spectroscopy or resistivity studies could not be performed to confirm the oxidation states, due to the inability to synthesize phase-pure bulk samples.

CONCLUSIONS

Two new compounds with infinite Fe-Se tetrahedral components are reported. Using two types of counter-ions, positively charged *tris*-ethylenediamine complexes and negatively charged chloride anions allowed us to stabilize new arrangements of linear $FeSe_2$ tetrahedral chains in the crystal structure of $[Fe(en)_3]_3(FeSe_2)_4Cl_2$ and novel 2D puckered $Fe_{14}Se_{21}$ layers in the crystal structure of $[Fe(en)_3]_4(Fe_{14}Se_{21})Cl_2$. Both compounds are mixed-valent. For $[Fe(en)_3]_3(FeSe_2)_4Cl_2$, Mössbauer spectroscopy confirmed a +2 oxidation state for Fe in the *tris*-ethylenediamine complex and a +3 oxidation state for Fe in the tetrahedral chains. Magnetic characterizations indicate antiferromagnetic interactions within $FeSe_2$ tetrahedral chains, but no long-range magnetic ordering was detected down to 1.8 K. Weak *inter*chain AFM correlations mediated by the $[Fe(en)_3]^{2+}$ cations causes magnetic frustration, giving rise to a spin glass state. The more complex crystal structure of $[Fe(en)_3]_4(Fe_{14}Se_{21})Cl_2$ is expected to have mixed valent +2/+3 Fe atoms within the $Fe_{14}Se_{21}$ layers. The stabilization of novel structural fragments reveals the potential to use a cation/anion combination to produce novel magnetic Fe chalcogenides.

ASSOCIATED CONTENT

Supporting Information.

Table with summary of synthetic conditions and details of synthesis and characterization procedures, crystallographic files, additional X-ray diffraction figures, sample photographs, EDS spectra, SEM images, additional FTIR and AC magnetic measurement figures and selected structural data table for $[Fe(en)_3]_4(Fe_{14}Se_{21})Cl_2$. This material is available free of charge via the Internet at http://pubs.acs.org.

AUTHOR INFORMATION

Corresponding Author

Dr. Kirill Kovnir, kovnir@iastate.edu

Author Contributions

The manuscript was written through contributions of all authors.

Conflict of Interests

Authors declare no conflict of interests.

Funding Sources

This research was supported by National Science Foundation DMR-2003783 grant to KK. Magnetic characterization performed by JKC and MS were supported by NSF DMR-1905499. Low frequency FTIR work by L.L. and J.W. was supported by the Ames Laboratory, the US Department of Energy, Office of Science, Basic Energy Sciences, Materials Science and Engineering Division under contract No. DE-AC02-07CH11358. Use of the Advanced Photon Source, an Office of Science User Facility operated for the U.S. Department of Energy (DOE) Office of Science by Argonne National Laboratory, was supported by the U.S. DOE under Contract No. DE-AC02-06CH11357.

ACKNOWLEDGMENTS

The authors are thankful to Dr. W. Xu and Dr. A. Yakovenko (APS ANL) for help with collecting *in-situ* synchrotron XRD patterns, Dr. Brett Boote (Chemical Instrumentation Facility at ISU) for help with the FTIR measurements, Dr. Warren Straszheim for the access to SEM/EDS at MARL ISU, and Shannon Lee for EDS data collection.

REFERENCES

(1) Hsu, F.; Luo, J.; Yeh, K.; Chen, T.; Huang, T.; Wu, P. M.; Lee, Y.; Huang, Y.; Chu, Y.; Yan, D.; Wu, M. Superconductivity in the PbO-Type Structure α-FeSe. *Proc. Natl. Acad. Sci. U. S. A.* **2008**, *05*, 14262–14264.

(2) Huang, F. Observation of Superconductivity in Tetragonal FeS. *J. Am. Chem. Soc.* **2015**, *137*, 10148–10151.

(3) Greenfield, J. T.; Kamali, S.; Lee, K.; Kovnir, K. A Solution for Solution-Produced β-FeSe: Elucidating and Overcoming Factors That Prevent Superconductivity. *Chem. Mater.* **2015**, *27*, 588–596.

(4) Borg, C. K. H.; Zhou, X.; Eckberg, C.; Campbell, D. J.; Saha, S. R.; Paglione, J.; Rodriguez, E. E. Strong Anisotropy in Nearly Ideal Tetrahedral Superconducting FeS Single Crystals. *Phys. Rev. B* **2016**, *93*, 094522.

(5) Guo, Z.; Sun, F.; Yuan, W. Chemical Intercalations in Layered Transition Metal Chalcogenides: Syntheses, Structures, and Related Properties. *Cryst. Growth Des.* **2017**, *17*, 2238–2253.

(6) Vivanco, H. K.; Rodriguez, E. E. The Intercalation Chemistry of Layered Iron Chalcogenide Superconductors. *J. Solid State Chem.* **2016**, *242*, 3–21.

(7) Burrard-Lucas, M.; Free, D. G.; Sedlmaier, S. J.; Wright, J. D.; Cassidy, S. J.; Hara, Y.; Corkett, A. J.; Lancaster, T.; Baker, P. J.; Blundell, S. J.; Clarke, S. J. Enhancement of the Superconducting Transition Temperature of FeSe by Intercalation of a Molecular Spacer Layer. *Nat. Mater.* **2013**, *12*, 15–19.

(8) P Ying, E. T.; Chen, X. L.; Wang, G.; Jin, S. F.; Zhou, T. T.; Lai, X. F.; Zhang, H.; Wang, W. Y. Observation of Superconductivity at 30~46K in $A_xFe_2Se_2$ (A= Li, Na, Ba, Sr, Ca, Yb, and Eu). *Sci. Rep.* **2012**, *2*, 426–432.

(9) Paglione, J.; Greene, R. L. High-Temperature Superconductivity in Iron-Based Materials. *Nat. Phys.* **2010**, *6*, 645–658.

(10) Panda, S. K.; Dasgupta, I.; Saha-Dasgupta, T. Electronic Structure and Magnetism of K-Intercalated Iron Chalcogenides. *Phys. Rev. B - Condens. Matter Mater. Phys.* **2015**, *92*, 104421.

(11) Woodruff, D. N.; Schild, F.; Topping, C. V.; Cassidy, S. J.; Blandy, J. N.; Blundell, S. J.; Thompson, A. L.; Clarke, S. J. The Parent Li(OH)FeSe Phase of Lithium Iron Hydroxide Selenide Superconductors. *Inorg. Chem.* **2016**, *55*, 9886–9891.

(12) Sun, H.; Woodruff, D. N.; Cassidy, S. J.; Allcroft, G. M.; Sedlmaier, S. J.; Thompson, A. L.; Bingham, P. A.; Forder, S. D.; Cartenet, S.; Mary, N.; Ramos, S.; Foronda, F. R.; Williams, B. H.; Li, X.; Blundell, S. J.; Clarke, S. J. Soft Chemical Control of Superconductivity in Lithium Iron Selenide Hydroxides $Li_{1-X}Fe_X(OH)Fe_{1-Y}Se$. *Inorg. Chem.* **2015**, *54*, 1958–1964.

(13) Topping, C. V.; Kirschner, F. K. K.; Blundell, S. J.; Baker, P. J.; Woodruff, D. N.; Schild, F.; Sun, H.; Clarke, S. J. Coexistence of Magnetism and Superconductivity in Separate Layers of the Iron-Based Superconductor $Li_{1-X}Fe_X(OH)Fe_{1-Y}Se$. *Phys. Rev. B* **2017**, *95*, 134419.

(14) Ying, T.; Chen, X.; Wang, G.; Jin, S.; Lai, X.; Zhou, T.; Zhang, H.; Shen, S.; Wang, W. Superconducting Phases in Potassium-Intercalated Iron Selenides. *J. Am. Chem. Soc.* **2013**,

135, 2951–2954.

(15) Sedlmaier, S. J.; Cassidy, S. J.; Morris, R. G.; Drakopoulos, M.; Reinhard, C.; Moorhouse, S. J.; O'Hare, D.; Manuel, P.; Khalyavin, D.; Clarke, S. J. Ammonia-Rich High-Temperature Superconducting Intercalates of Iron Selenide Revealed through Time-Resolved in Situ X-Ray and Neutron Diffraction. *J. Am. Chem. Soc.* **2014**, *136*, 630–633.

(16) Wu, M.; Rhee, J.; Emge, T. J.; Yao, H.; Cheng, J. H.; Thiagarajan, S.; Croft, M.; Yang, R.; Li, J. A Low Band Gap Iron Sulfide Hybrid Semiconductor with Unique 2D $[Fe_{16}S_{20}]^{8-}$ Layer and Reduced Thermal Conductivity. *Chem. Commun.* **2010**, *46*, 1649–1651.

(17) Krzton-Maziopa, A.; Pesko, E.; Puzniak, R. Superconducting Selenides Intercalated with Organic Molecules: Synthesis, Crystal Structure, Electric and Magnetic Properties, Superconducting Properties, and Phase Separation in Iron Based-Chalcogenides and Hybrid Organic-Inorganic Superconductors. *J. Phys. Condens. Matter* **2018**, *30*, 243001.

(18) Zhou, X.; Wilfong, B.; Liou, S. C.; Hodovanets, H.; Brown, C. M.; Rodriguez, E. E. Proton and Ammonia Intercalation into Layered Iron Chalcogenides. *Chem. Commun.* **2018**, *54*, 6895–6898.

(19) Krzton-Maziopa, A.; Pomjakushina, E. V.; Pomjakushin, V. Y.; Von Rohr, F.; Schilling, A.; Conder, K. Synthesis of a New Alkali Metal-Organic Solvent Intercalated Iron Selenide Superconductor with $T_c \sim 45$K. *J. Phys. Condens. Matter* **2012**, *24*, 382202.

(20) Gao, Z.; Zeng, S.; Zhu, B.; Li, B.; Hao, Q.; Hu, Y.; Wang, D.; Tang, K. A FeSe-Based Superconductor $(C_2H_8N_2)_xFeSe$ with Only Ethylenediamine Intercalated. *Sci. China Mater.* **2018**, *61*, 977–984.

(21) Li, J.; Chen, Z.; Wang, R. J.; Proserpio, D. M. Low Temperature Route towards New Materials: Solvothermal Synthesis of Metal Chalcogenides in Ethylenediamine. *Coord. Chem. Rev.* **1999**, *190–192*, 707–735.

(22) Wu, D.; Guo, Z.; Liu, N.; Zhou, L.; Mao, Y.; Wan, L.; Sun, F.; Yuan, W. A New Intercalated Iron Sulfide $(C_2H_8N_2)_{0.4}Fe_2S_2$ from Solvothermal Route: Synthesis, Structure and Tunable Magnetism. *Inorg. Chem. Commun.* **2018**, *91*, 72–76.

(23) Li, T.; Liu, Y.-H.; Porter, S.; Goldberger, J. E. Dimensionally Reduced One-Dimensional Chains of $TiSe_2$. *Chem. Mater.* **2013**, *24*, 1477–1479.

(24) Morasse, R. A. L.; Li, T.; Baum, Z. J.; Goldberger, J. E. Rational Synthesis of Dimensionally Reduced TiS_2 Phases. *Chem. Mater* **2014**, *26*, 4776−4780.

(25) Li, T.; Liu, Y.-H.; Chitara, B.; Goldberger, J. E. Li Intercalation into 1D TiS_2(en) Chains. *J. Am. Chem. Soc.* **2014**, *136*, 2986–2989.

(26) Pak, C.; Kamali, S.; Pham, J.; Lee, K.; Greenfield, J. T.; Kovnir, K. Chemical Excision of Tetrahedral $FeSe_2$ Chains from the Superconductor FeSe: Synthesis, Crystal Structure, and Magnetism of $Fe_3Se_4(en)_2$. *J. Am. Chem. Soc.* **2013**, *135*, 19111–19114.

(27) Greenfield, J. T.; Pak, C.; Kamali, S.; Lee, K.; Kovnir, K. Control over Connectivity and Magnetism of Tetrahedral $FeSe_2$ Chains through Coordination Fe–Amine Complexes. *Chem. Commun.* **2015**, *51*, 5355–5358.

(28) Han, I.; Jiang, Z.; dela Cruz, C.; Zhang, H.; Sheng, H.; Bhutani, A.; Miller, D. J.; Shoemaker, D. P. Accessing Magnetic Chalcogenides with Solvothermal Synthesis: $KFeS_2$ and KFe_2S_3. *J. Solid State Chem.* **2018**, *260*, 1–6.

(29) Bronger, W.; Kyas, A.; Müller, P. The Antiferromagnetic Structures of $KFeS_2$, $RbFeS_2$, $KFeSe_2$, and $RbFeSe_2$ and the Correlation between Magnetic Moments and Crystal Field Calculations. *J. Solid State Chem.* **1987**, *70*, 262–270.

(30) Seidov, Z.; Krug von Nidda, H.-A.; Tsurkan, V.; Filippova, I.; Günther, A.; Najafov, A.; Aliyev, M. N.; Vagizov, F. G.; Kiiamov, A. G.; Tagirov, L. R.; Gavrilova, T.; Loidl, A. Magnetic Properties of Chain Antiferromagnets $RbFeSe_2$, $TlFeSe_2$, and $TlFeS_2$. *Bull. Russ. Acad. Sci. Phys.* **2017**, *81*, 885–887.

(31) Stahl, J.; Shlaen, E.; Singer, H.; Johrendt, D. Systematic Dimensional Reduction of the Layered β-FeSe Structure by Solvothermal Synthesis. *Dalt. Trans.* **2018**, *47*, 3264–3271.

(32) Emsley, J. *The Elements*; Clarendon Press: Oxford, UK, **1998**.

(33) Lu, J.; Xie, Y.; Xu, F.; Zhu, L. Study of the Dissolution Behavior of Selenium and Tellurium in Different Solvents - A Novel Route to Se, Te Tubular Bulk Single Crystals. *J. Mater. Chem.* **2002**, *12*, 2755–2761.

(34) Gorer, S.; Hodes, G. Quantum Size Effects in the Study of Chemical Solution Deposition Mechanisms of Semiconductor Films. *J. Phys. Chem.* **1994**, *98*, 5338–5346.

(35) Halcrow, M. A. *Spin-Crossover Materials: Properties and Applications*; John Wiley & Sons, Ltd.: Oxford, UK, **2013**.

(36) Oliver, J. D.; Hutchinson, B. B.; Mullica, D. F.; Milligan, W. O. Iron-Nitrogen Bond Lengths in Low-Spin and High-Spin Iron (II) Complexes with Poly (Pyrazolyl) Borate Ligands. *Inorg. Chem.* **1980**, *19*, 165–169.

(37) Smeets, V.; Wolff, M.; Wolny, J. A.; Schünemann, V.; Dîrtu, M. M.; Ge, J. Y.; Vanacken, J.; Moshchalkov, V.; Garcia, Y. Spin State Crossover, Vibrational, Computational, and Structural Studies of Fe^{II} 1-Isopropyl-1*H*-Tetrazole Derivatives. *Eur. J. Inorg. Chem.* **2018**, *2018*, 394–413.

(38) Brese, N. E.; O'Keeffe, M. Bond-valence Parameters for Solids. *Acta Crystallogr. Sect. B* **1991**, *47*, 192–197.

(39) Lemmon, E. W.; McLinden, M. O.; Friend, D. G. Thermophysical Properties of Fluid Systems. In *NIST Chemistry WebBook: NIST Standard Reference Database Number 69*; Eds.; P.J. Linstrom and W.G. Mallard, National Institute of Standards and Technology: Gaithersburg, MD, **2017**; p 20899.

(40) Cooke, K.; Olenev, A. V.; Kovnir, K. Tris(ethylenediamine)Cobalt(II) Dichloride. *Acta Crystallogr. Sect. E Struct. Reports Online* **2013**, *69*, 332.

(41) Krishnan, K.; Plane, R. A. Raman and Infrared Spectra of Complexes of Ethylenediamine with Zinc(II), Cadmium(II), and Mercury(II). *Inorg. Chem.* **1966**, *5*, 852–857.

(42) Norani, N.; Rahemi, H.; Tayyari, S. F.; Riley, M. J. Conformational Stabilities, Infrared, and Vibrational Dichroism Spectroscopy Studies of Tris(ethylenediamine) Zinc(II) Chloride. *J. Mol. Model.* **2009**, *15*, 25–34.

(43) Bennett, A. M. A.; Foulds, G. A.; Thornton, D. A. The IR Spectra of Ethylenediamine Complexes-I. The *Tris*(ethylenediamine) Complexes of First Transition Series Metal(II) Sulphates. *Spectrochim. Acta Part A Mol. Spectrosc.* **1989**, *45*, 219–223.

(44) Kamali-M., S.; Ericsson, T.; Wäppling, R. Characterization of Iron Oxide Nanoparticles by Mössbauer Spectroscopy. *Thin Solid Films* **2006**, *515* (2 SPEC. ISS.), 721–723.

(45) Kamusella, S.; To Lai, K.; Harnagea, L.; Beck, R.; Pachmayr, U.; Singh Thakur, G.; Klauss, H. H. ^{57}Fe Mössbauer Spectroscopy on Iron Based Pnictides and Chalcogenides in Applied Magnetic Fields. *Phys. Status Solidi Basic Res.* **2017**, *254*, 1600160.

(46) Seidov, Z.; Krug Von Nidda, H.-A.; Tsurkan, V.; Filippova, I. G.; Günther, A.; Gavrilova, T. P.; Vagizov, F. G.; Kiiamov, A. G.; Tagirov, L. R.; Loidl, A. Magnetic Properties of the Covalent Chain Antiferromagnet $RbFeSe_2$. *Phys. Rev. B* **2016**, *94*, 134414.

(47) Umemura, Y.; Minai, Y.; Tominaga, T. Structural Distortion of 6-Coordinated Fe(II) Complexes in Zeolite Y. *J. Phys. Chem. B* **1999**, *103*, 647–652.

(48) Brozek, C. K.; Ozarowski, A.; Stoian, S. A.; Dincă, M. Dynamic Structural Flexibility of Fe-MOF-5 Evidenced by ^{57}Fe Mössbauer Spectroscopy. *Inorg. Chem. Front.* **2017**, *4*, 782–788.

(49) Mydosh, J. A. *Spin Glasses : An Experimental Introduction*; Taylor & Francis: London; Washington DC, **1993**.

(50) Du, F.; Huang, Z. F.; Wang, C. Z.; Meng, X.; Chen, G.; Chen, Y.; Feng, S. H. Spin-Glass-like Behavior in Rhombohedral $Li(Mn,Cr)O_2$. *J. Appl. Phys.* **2007**, *102*, 113906.

(51) Chen, H.; Yang, X.; Zhang, P.-S.; Liang, L.; Hong, Y.-Z.; Wei, Y.-J.; Chen, G.; Du, F.; Wang, C.-Z. Observation of Spin Glass Transition in Spinel $LiCoMnO_4$. *Chinese Phys. B* **2015**, *24*, 127501.

(52) Kovnir, K.; Garlea, V. O.; Thompson, C. M.; Zhou, H. D.; Reiff, W. M.; Ozarowski, A.; Shatruk, M. Spin-Glass Behavior in $LaFe_xCo_{2-x}P_2$ Solid Solutions: Interplay between Magnetic Properties and Crystal and Electronic Structures. *Inorg. Chem.* **2011**, *50*, 10274–10283.

(53) Caron, J. M.; Neilson, J. R.; Miller, D. C.; Arpino, K.; Llobet, A.; McQueen, T. M. Orbital-

Selective Magnetism in the Spin-Ladder Iron Selenides $Ba_{1-x}K_xFe_2Se_3$. *Phys. Rev. B - Condens. Matter Mater. Phys.* **2012**, *85*, 180405.

(54) Klepp, K. O.; Sparlinek, W.; Boiler, H. Mixed Valent Ternary Iron Chalcogenides: AFe_2X_3 (A = Rb, Cs; X = Se, Te). *J. Alloy. Compd.* **1996**, *238*, 1–5.

(55) Koz, C.; Schmidt, M.; Borrmann, H.; Burkhardt, U.; Rößler, S.; Carrillo-Cabrera, W.; Schnelle, W.; Schwarz, U.; Grin, Y. Synthesis and Crystal Growth of Tetragonal β-$Fe_{1.00}Se$. *Zeitschrift fur Anorg. und Allg. Chemie* **2014**, *640*, 1600–1606.

For Table of Contents Only

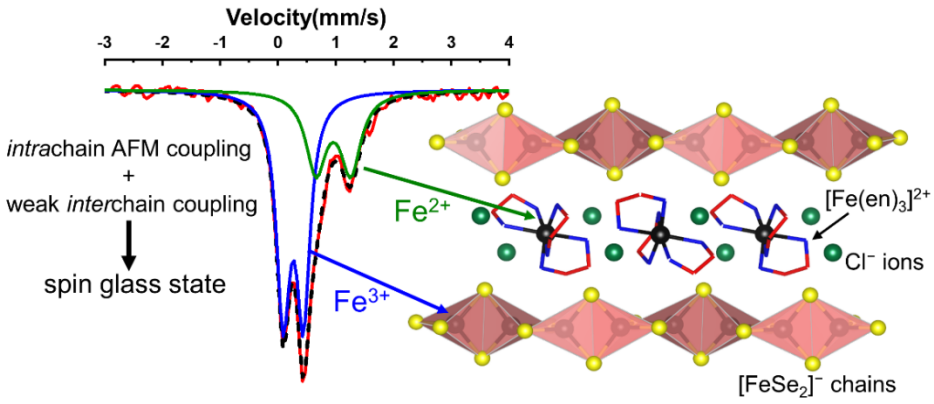

Novel low-dimensional mixed-valent compounds, 1D $[Fe(en)_3]_3(FeSe_2)_4Cl_2$ (*en* = ethylenediamine) and 2D $[Fe(en)_3]_4(Fe_{14}Se_{21})Cl_2$ have been synthesized by solvothermal methods. In both compounds, Fe-Se fragments, either tetrahedral chains or unique puckered layers, are stabilized by two types of ions, $[Fe(en)_3]^{2+}$ cations and Cl^- anions. Weak *inter*chain antiferromagnetic correlations in $[Fe(en)_3]_3(FeSe_2)_4Cl_2$, give rise to a spin glass state. This work reveals the potential of using cation/anion combinations to stabilize novel iron-based magnetic chalcogenides.